

RESEARCH ARTICLE **OPEN ACCESS**

Application of Non-Isothermal Network Theory With Curved-Channel Element Characteristics to Predict Melt Conveying in High-Performance Single-Screw Extruders

Daniel Herzog¹  | Wolfgang Roland² | Christian Marschik³  | Gerald Berger-Weber¹¹Institute of Polymer Processing and Digital Transformation, Johannes Kepler University Linz, Linz, Austria | ²Independent Researcher, Altenfelden, Austria | ³Competence Center CHASE GmbH, Linz, Austria**Correspondence:** Daniel Herzog (daniel.herzog@jku.at)**Received:** 16 December 2025 | **Revised:** 27 February 2026 | **Accepted:** 3 March 2026**Keywords:** flow simulation | lumped-parameter models | screw design | troubleshooting | wave-dispersion screws

ABSTRACT

High-performance screws, such as barrier and wave-dispersion screws, are becoming increasingly popular in single-screw extrusion due to their improved melting behavior, mixing action, and energy efficiency. In contrast to time-consuming experimental trials and full-scale numerical simulations, network theory offers a fast and user-friendly alternative to analyze the melt conveying behavior of these screws. However, traditional models for flat channels introduce significant errors to this theory when applied to deep channel sections in high-performance screws. To resolve this problem, an advanced calculation tool based on non-isothermal network-theory is proposed, which features novel regression models that fully capture the effects of shear-thinning, channel curvature and undercut flights on the flow. The effectiveness of this approach is then tested by recalculating experiments on a high-speed, small-scale industrial extruder. In most cases, the computed pressure profiles closely match the experimental values, and the advanced models generally provide more accurate predictions compared to their most potent predecessors. The enhanced predictive power of the advanced network-based calculations can aid in more efficient design and troubleshooting of high-performance single-screw extruders, thus contributing to more reliable and sustainable extrusion processes.

1 | Introduction

Single-screw extruders are involved in manufacturing plastic products at various stages along the value chain: These include post-reactor processing, continuous production of films, pipes, profiles and sheets, as well as mechanical recycling of plastic waste. All these processes require the extruder to pump the polymer in its molten state through a shaping die. While transported, the polymer melt must be consistently and sufficiently pressurized to provide stable material supply at the desired output rate. At the same time, the melt temperature must be limited for smooth shaping operations, saving energy, and preventing the polymer from degrading. Furthermore, a materially and thermally homogeneous melt is crucial to ensure dimensional stability and high product quality. Yet these basic tasks

become increasingly difficult to fulfil as economic pressure and sustainable development goals add further demands on energy efficiency and processability of variable feedstock. In many cases, conventional screw designs no longer fully meet all these requirements.

Responding this engineering challenge, several high-performance screw designs have been proposed to improve the pumping and mixing capabilities of single-screw extruders. The double-wave (DW) screw invented by Kruder [1] exhibits two wave-like channels that oscillate in depth out of phase and are separated by a barrier flight. The alternately tapering channels force the polymer melt to pass the tight wave peaks multiple times, leading to dispersion of solid particles. Repeated splitting of the flow between the wave peaks and the barrier flight

This is an open access article under the terms of the [Creative Commons Attribution](https://creativecommons.org/licenses/by/4.0/) License, which permits use, distribution and reproduction in any medium, provided the original work is properly cited.

© 2026 The Author(s). *Journal of Polymer Science* published by Wiley Periodicals LLC.

clearance also promotes distributive mixing. With deep and shallow channel sections located next to each other, stable pumping action can be achieved at lower power input compared to standard metering screws. The energy-transfer (ET) screw patented by Chung and Barr [2] rests on the same principle with one key distinction: Both flights are no longer uniform but selectively undercut to guide the melt to the channel upstream when crossing the flights. This allows for even lower power consumption and improved mixing compared to the double-wave screw at the expense of pumping capability. Since then, numerous advanced versions have been developed for both screw concepts to address the shortcomings of the originals. However, the expected performance boosts are only achieved with a proper dimensioning of the screw. As knowledge of the complex flow pattern in wave-dispersion screws is scarce, finding an acceptable design usually necessitates multiple experimental trials. Fast and reliable prediction models on the melt conveying behavior of these screws would reduce the need for such trials and thus help to exploit the potential of high-performance screws in polymer extrusion.

The mathematical description of melt conveying in single-screw pumps was initiated by Rowell and Finlayson [3, 4] and expanded by several other researchers [5–7] for an isothermal flow of Newtonian fluids in constant-shaped channels. These pioneering studies present exact analytical equations for the linear superimposed drag and pressure flows in the down-and cross-channel directions. However, the shear-rate-dependent viscosity of most polymer melts induces a coupling of the flow components, which generally requires numerical methods to obtain realistic results. Steadily improving computational capabilities enabled increasingly sophisticated fluid dynamics simulations of the polymer melt flow through both conventional [8, 9] and wave-type screw channels [10–12]. Though providing close and detailed representations of the three-dimensional flow patterns and temperature distributions inside the extruder, such simulations take several days to prepare and evaluate for long or complex-shaped extruder zones. Hence, these simulation times are unacceptable for time-critical extruder design and troubleshooting tasks.

The shortcomings of exact analytical and full-scale numerical methods prompted the derivation of analytical regression models from numerically simulated melt conveying characteristics of single-screw extruders. These regression models describe the conveying behavior of short screw segments and have been implemented into various segmented extruder calculations [13–15] to account for variable dimensions and material properties along the screw. To date, the most advanced approach invokes the principles of network theory (as proposed in [16–18]), which additionally couples the local channel and leakage flows through grid-like connections between conveying elements. This approach has already been applied to high-performance extruders with double-wave screws [17] and barrier screws in grooved plasticizing barrels [19]. The predictive capability for high-performance extrusion conditions, however, is still constrained by the validity of the regression models in use: Most importantly, none of these adequately captures three-dimensional channel curvature, which introduces significant errors for deep-flighted screw segments. Moreover, the network-theory-based calculations have been tested only on a limited number of high-performance extrusion conditions: For instance, junctions

of metering and wave zones, energy-transfer zones, and non-isothermal flows in wave zones are yet to be evaluated.

This research work is intended to expand the applicability of fast-computing network theory to a wider range of melt-conveying zones in single-screw extrusion. To this end, we propose an upgraded computational routine that addresses (i) channel curvature, (ii) thermal behavior of screws with multiple undercut flights, and (iii) combinations of standard and high-performance metering sections. The effectiveness of this new version is then validated against experiments on a small-scale industrial extruder with different high-performance screw designs. This paper is thus structured as follows: Section 2 reports the materials, screws, and experimental tests employed in this validation study. Section 3 explains the theoretical principles and computational workflow of the non-isothermal network analysis routine, with special focus on the modifications for increased accuracy. Section 4 then presents and discusses the results from the advanced network analysis compared to the experiments and previous versions. Finally, the paper summarizes the key findings of the study and outlines the potential of the calculation tool for future industrial applications.

2 | Extrusion Experiments

2.1 | Materials

Two commodity polymer grades were processed within this validation study: (i) the high-density polyethylene HDPE HE3493LS-H used for pressure pipes, and (ii) the polypropylene random copolymer PP RD204CF as cast film material. Both grades were supplied by the company Borealis GmbH (Linz, Austria).

For modeling the non-isothermal flow of the polymer melts in the extruder accurately, at least three material properties needed to be known: (i) the shear-rate and temperature-dependent shear viscosity, (ii) the pressure- and temperature-dependent density, and (iii) the specific heat capacity. Heat conduction was not considered in the calculations, as the polymer melt flows in our study are largely dominated by convection and viscous dissipation (a detailed discussion is given in Section 3.1). The viscosities of the HDPE pipe grade were measured on a high-pressure capillary rheometer Rheograph 2002 with a slit die and a subsequent Weissenberg-Rabinowitsch correction [20]. The viscosity data for the PP film grade were obtained from small-amplitude oscillatory shear (SAOS) measurements on an Anton Paar MCR 302 parallel-plate rheometer, applying the Cox-Merz rule [21]. The shear-thinning behavior of the polymer melts was then described by the Bird-Carreau-Yasuda model with time-temperature superposition [22, 23]

$$\eta(\dot{\gamma}, T) = a_T(T) \left[\eta_\infty + (\eta_0 - \eta_\infty) \left(1 + (a_T(T) \lambda \dot{\gamma})^a \right)^{\frac{n_{CY}-1}{a}} \right] \quad (1)$$

considering the temperature dependence by a shift factor a_T . Since stronger temperature variations were expected for the higher viscous HDPE, the Arrhenius equation was applied to the temperature shift in this case,

$$a_T(T) = \exp\left(\frac{E_a}{R} \left(\frac{1}{T} - \frac{1}{T_{ref}}\right)\right) \quad (2)$$

whereas an exponential shift factor was employed for the lower viscous PP:

$$a_T(T) = \exp(-\beta (T - T_{ref})). \quad (3)$$

The polymer densities under processing conditions were characterized using a separate measuring chamber of the high-pressure capillary rheometers Rheograph 2002 for the HDPE and Rheograph 25 for the PP, respectively (Göttfert, Buchen,

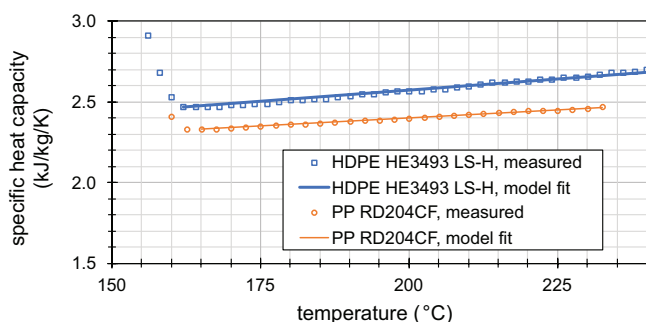


FIGURE 1 | Measured specific heat capacities of the polymer melts (dots) and model fits (lines) as functions of temperature.

TABLE 1 | Rheological model parameters of the polymer melts.

HDPE HE3493LS-H			PP RD204CF		
η_0	2.51×10^6	Pa s	η_0	1300	Pa s
η_∞	0	Pa s	η_∞	0	Pa s
λ	277	s	λ	0.0272	s
n_{CY}	0.277		n_{CY}	0.273	
a	2.08		a	0.619	
E_a	2.63×10^4	$\text{J mol}^{-1} \text{K}^{-1}$	β	0.0212	K^{-1}
T_{ref}	200	$^\circ\text{C}$	T_{ref}	240	$^\circ\text{C}$

TABLE 2 | Thermomechanical model parameters of the polymer melts.

HDPE HE3493LS-H			PP RD204CF		
b_1	0.00126	m^3/kg	b_1	0.00128	m^3/kg
b_2	9.03×10^{-7}	$\text{m}^3 \text{kg}^{-1} \text{K}^{-1}$	b_2	1.01×10^{-6}	$\text{m}^3 \text{kg}^{-1} \text{K}^{-1}$
b_3	4.29×10^7	Pa	b_3	6.34×10^7	Pa
b_4	-0.00517	K^{-1}	b_4	0.00355	K^{-1}
b_5	122	$^\circ\text{C}$	b_5	122	$^\circ\text{C}$
b_6	2.99×10^{-7}	K Pa^{-1}	b_6	2.50×10^{-7}	K Pa^{-1}
c_{p0}	2470	$\text{J kg}^{-1} \text{K}^{-1}$	c_{p0}	2330	$\text{J kg}^{-1} \text{K}^{-1}$
c_{pk}	2.78	$\text{J kg}^{-1} \text{K}^{-2}$	c_{pk}	2.03	$\text{J kg}^{-1} \text{K}^{-2}$
T_0	162	$^\circ\text{C}$	T_0	165	$^\circ\text{C}$

Germany). Their variation with temperature and pressure was mapped by the Tait equation [24] for the liquid state.

$$\rho(p; T > b_5 + b_6 p) = \frac{1}{(b_1 + b_2 (T - b_5)) \left[1 - 0.0894 \ln \left(1 + \frac{p}{b_3 \exp(b_4 (b_5 - T))} \right) \right]} \quad (4)$$

Moreover, differential scanning calorimetry was performed with a heating rate of 10K/min according to the ISO 11357 standard [25] to determine the specific heat capacities of the molten polymers, which were modeled as linear functions of temperature:

$$c_p(T) = c_{p,0} + c_{p,k} (T - T_0), \quad (5)$$

as clearly reflected in the data series for both materials (Figure 1) and further supported by the investigations of Dörner [12].

The rheological and thermomechanical model parameters are listed in Tables 1 and 2, respectively. They were determined by minimizing the total normalized squared error (TNSE) on the measurements above the melting range using the Generalized Reduced Gradient (GRG) Nonlinear solver of Microsoft Excel. The solver was run without constraints, single start, forward differencing, and a convergence threshold of 0.0001.

An impression of the flow behavior of the polymer melts is given in Figure 2. Their viscosities cover several decades within the expected shear rate range for high-performance extrusion that is shown in the plots. The materials also strongly differ in their absolute viscosities as well as in their shear-thinning characteristics. Hence, the polymer melts are likely to experience distinct flow conditions in the extruder.

2.2 | Equipment

2.2.1 | Extruder

The extrusion tests were conducted on a 45mm diameter high-speed single-screw extruder from Krauss Maffei GmbH (Hanover, Germany) with a gearless drive of 926 rpm nominal

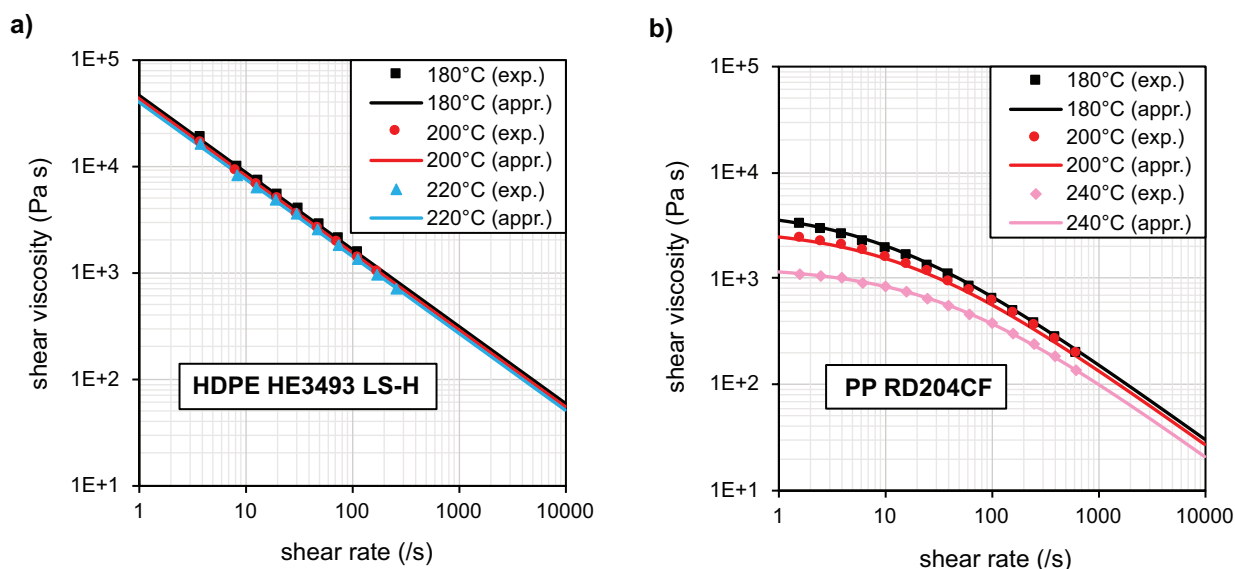


FIGURE 2 | Measured viscosities (symbols) and fitted viscosity curves for the HDPE pipe grade (a) and the PP film grade (b) at typical processing temperatures.

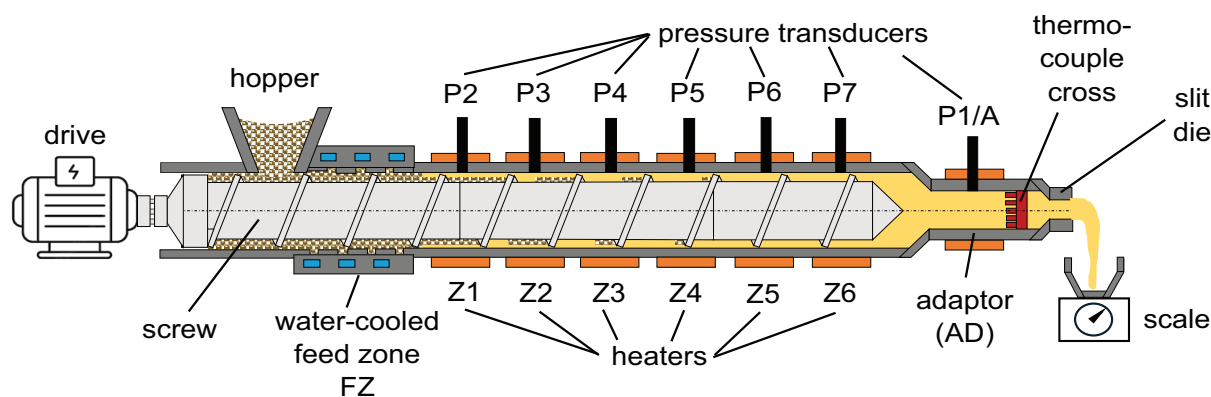


FIGURE 3 | Schematic illustration of the experimental extrusion setup.

TABLE 3 | Structural parameters of the grooves.

Parameter	Value	Unit
Number of grooves	6	
Axial length after the hopper	174.2	mm
Initial groove depth (at the hopper front edge)	3.5	mm
Groove width	8	mm
Groove pitch (left-handed)	144	mm

speed and 3063 Nm nominal torque. The extrusion assembly is schematically depicted in Figure 3. Along a total processing length of 1845 mm (41D) measured from the hopper front edge, the extruder accommodated a water-cooled feeding zone with a helically grooved bushing, followed by a smooth section with six instrumented heaters and cooling fans for controlling the barrel temperature. The structural parameters of the grooves, which were symmetrically arranged around the circumference

and constantly tapering axially, are given in Table 3. In downstream direction, the extruder was attached to a slit die through an adaptor and a throttle block to adjust the back pressure at the screw tip. A measuring cross consisting of 13 thermocouples around the circumference (Figure 4) was further placed between adaptor and throttle block to record the radial melt temperature distribution at the extruder outlet. The temperatures of the extruder zones were set according to Table 4, complying with the recommended processing range of the extruder and the respective material.

The melt pressure was recorded by seven piezoresistive transducers inserted through 1/2"-UNF holes at the adaptor (P1/A) and along the heated portion of the extruder (P2–P7). The measurement positions and specifications of the sensors are listed in Table 5. The sensors P2–P5 were specified with reinforced membranes and a measuring range up to 2000 bar to withstand the high pressures close to the groove end. For the remaining sensors further downstream, where less extreme pressures were expected, the chosen measuring range was successively lowered for more precise resolution.

2.2.2 | Screws

As this study focuses on the melt conveying behavior in extrusion, a modular screw configuration was employed consisting of two components: (i) a 29D long, double-flighted barrier screw for feeding and plastification, and (ii) four 12D long, exchangeable screw extensions in the metering section. The screw parts were assembled by a left-handed threaded joint that tightened under the torsional load on the rotating screw. The double-flighted barrier screw concept was preferred due to its superior plastification performance in previous experiments [26], aiming for fully molten plastic throughout the metering section. The screw extensions were (i–ii) two single-flighted, deep-channel metering zones (M1, M2) of different depth and pitch, (iii) a double-wave zone (DW), and (iv) an energy-transfer zone (ET) of intermediate pitch. Table 6 lists the main dimensions and geometrical ratios of the screw extensions, and Figure 5 plots the variable channel depths and flight clearances of the wave-type designs. As evident from the figure and table, the double-wave and energy-transfer screws were designed identically except for their flight clearances to investigate the differences between the screw concepts. All screw extensions further exhibited a short decompression

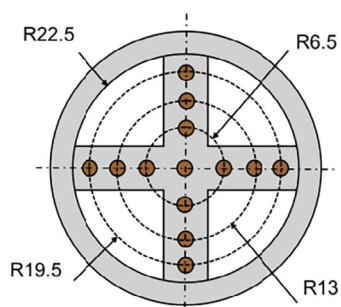


FIGURE 4 | Thermocouple arrangement in the measuring cross (dimensions in mm).

TABLE 4 | Set temperature profiles of the extrusion equipment.

Zone	Feed	Z1	Z2	Z3	Z4	Z5	Z6	Adaptor	Die
Axial position (mm)	0–192	223–475	481–733	739–991	997–1249	1255–1507	1537.5–1791.5	1845–1892	1845–2178
Temperature for HDPE (°C)	40	220	215	210	200	200	200	200	200
Temperature for PP (°C)	40	220	230	240	240	240	240	240	240

TABLE 5 | Positions and specifications of the pressure transducers.

Transducer	P2	P3	P4	P5	P6	P7	P1/A ^a
Axial position (mm)	370	628	886	1144	1402	1734	1910
Measuring range (bar)	0–2000	0–2000	0–2000	0–2000	0–1000	0–700	0–700
Signal range	0–10V	0–10V	0–10V	0–10V	4–20 mA	4–20 mA	4–20 mA

^aLocated in the adaptor downstream from the screw.

at the beginning, which explains the ranges for the channel depth ratio and channel aspect ratio of the M1 and M2 screw. The screw structures altogether covered a broad range of channel depth ratios, screw pitch ratios, and channel depth ratios observed in high-speed extrusion. In contrast to past investigations, more emphasis was placed on deeper screws to test the ability of our advanced melt conveying calculation to account for channel curvature.

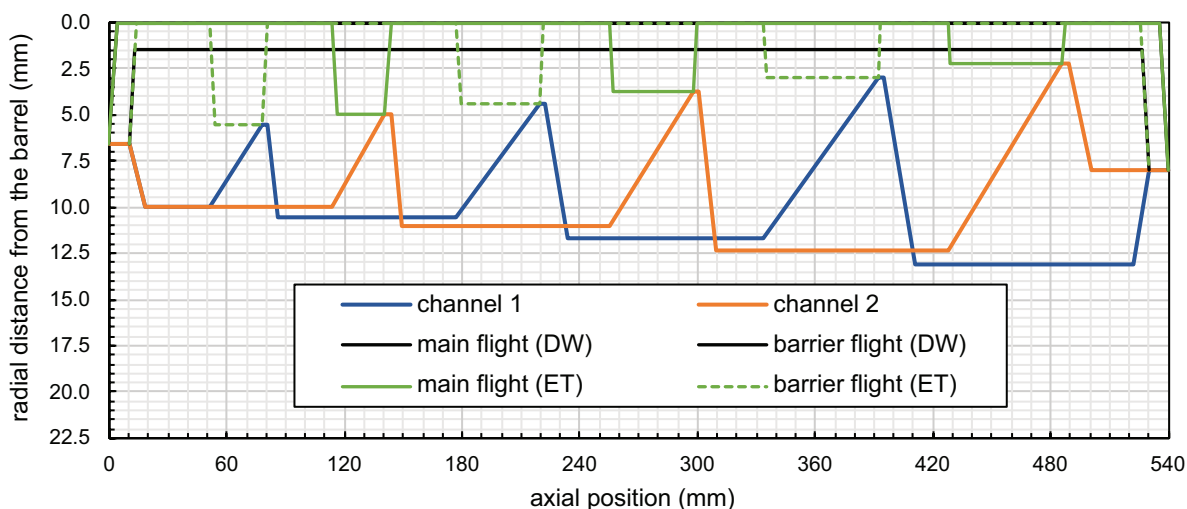
2.3 | Procedure

Starting from the first test point at 50 rpm, the screw speed was successively increased by steps of 25 rpm until 150 rpm. Beyond this limit, signs of incomplete melting had already become evident. The process was allowed to reach an equilibrium for at least 15 min after startup and at least 10 min between operating points, ensuring flood-fed operation at a constant adaptor pressure of 280 bar. Once the process had settled at a steady state, the extruded mass was measured by a differential weight scale (Kern Balance Connection) over a 90 s interval with 9 s sampling time for the high-viscous HDPE and a 45 s interval with 3 s sampling time for the low-viscous PP, respectively. The different measuring and sampling intervals for the materials were motivated by the periodic pulses from the folding melt strand in the collection container, which exhibited lower frequencies for the more viscous HDPE. The mass throughput was then determined from linear regression on the respective time series data of the scale. The sensor signals for the screw speed, melt temperatures, and pressures at P1/A to P2–P5 were processed directly at the extruder control unit at a sampling interval of 1 s. Extracting the pressure signals from P6 and P7 was achieved by an external screen recorder (JUMO Logoscreen NT). For all signals, the mean values and standard deviations were computed within each throughput measuring interval to reduce and monitor the impact of process fluctuations. Due to the larger sampling interval of 30 s of the external recorder, two sampling points

TABLE 6 | Main dimensions and geometric ratios of the screw extensions.

Screw		M1	M2	DW	ET
Flighted length	mm	540	540	540	540
Number of flights		1	1	1 pair	1 pair
Inlet channel depth	mm	6.6	6.6	6.6	6.6
Channel depth after decompression	mm	12	8.5	10	10
Outlet channel depth	mm	12	8.5	8	8
Decompression length after joint	mm	40	40	8	8
Main flight clearance	mm	0.1	0.1	0.1	Variable (≥ 0.1)
Barrier flight clearance	mm	—	—	1.5	Variable (≥ 0.1)
Pitch	mm	54	99	72	72
Flight width	mm	4	4	3	3
Flight flank radius	mm	2	2	2	2
Flight taper		5°	5°	5°	5°
Flight transition angle		60°	60°	60°	60°
Channel depth ratio (channel depth/inner barrel diameter)		[0.14; 0.27]	[0.14; 0.19]	[0.05; 0.29]	[0.05; 0.29]
Screw pitch ratio (pitch/inner barrel diameter)		1.2	2.2	1.6	1.6
Channel aspect ratio (channel depth/channel width at the barrel)		[0.14; 0.26]	[0.08; 0.11]	[0.07; 0.46]	[0.07; 0.46]

Note: The bold values refer to the ranges of the characteristic dimensionless parameters of the screw channels used in the experiments.

**FIGURE 5** | Axial profiles of the channel depths and flight clearances in the wave-type screw extensions.

immediately before and one sampling point immediately after the throughput measurement were included in the pressure evaluation from P6 and P7. The melt temperature at the screw tip was finally estimated as a mass-flow weighted average of the measured temperature distribution

$$T_{out} = \sum_{k=1}^4 X_k T_k \quad (6)$$

after arithmetic averaging across the circumference, using the weighting factors

$$X_k = \frac{1+3n}{1+n} \left[\left(\frac{2r_{k+1}}{D} \right)^2 - \left(\frac{2r_k}{D} \right)^2 \right] - \frac{2n}{1+n} \left[\left(\frac{2r_{k+1}}{D} \right)^{\frac{1+3n}{n}} - \left(\frac{2r_k}{D} \right)^{\frac{1+3n}{n}} \right] \quad (7)$$

according to Hörmann [27] for each layer between the radial measurement positions r_k . The power-law indices n for the temperature evaluation were obtained from separate fits of the viscosity data, considering only shear rates above 10/s.

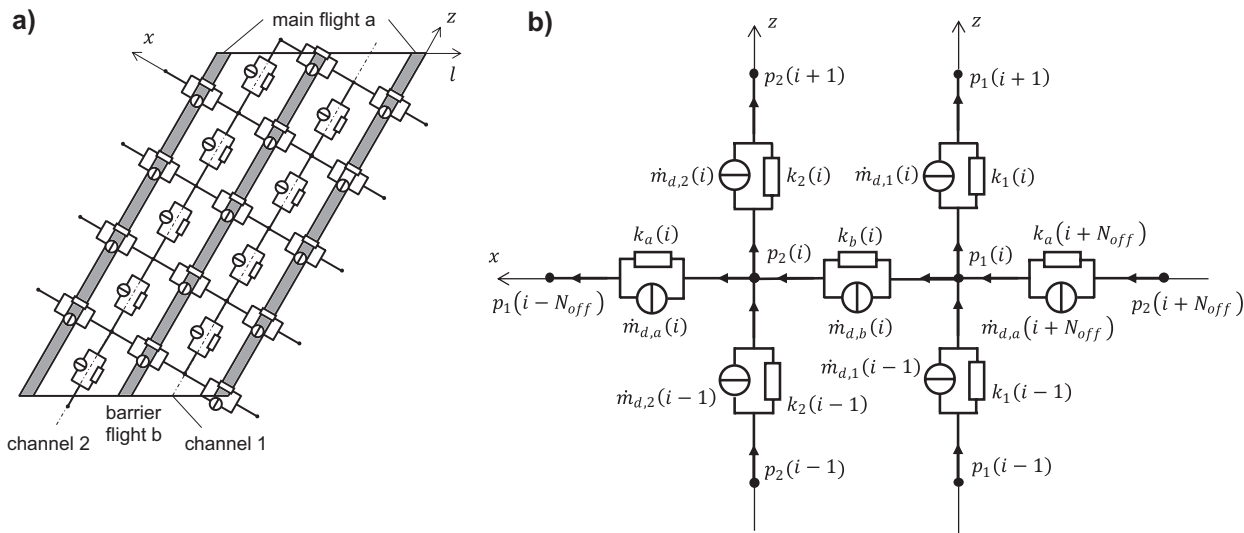


FIGURE 6 | Structure of the hydraulic network along a wave zone (a) and its equivalent circuit diagram (b): z ...down-channel direction, x ...cross-channel direction, l ...axial/extrusion direction. Reproduced under the terms of the CC-BY license [17]. 2020, Marschik et al., published by MDPI.

3 | Calculation Scheme

3.1 | Network Theory

From the various flow simulation methods available, network theory was employed to predict the melt pressures, melt temperatures, and mass flow rates from the experiments. Though commonly applied for the analysis of electrical circuits, network theory can be likewise transferred to hydraulic or thermal systems, such as the metering zone of a single-screw extruder. The main principle behind this approach is as follows: The extruder chamber is partitioned into an array of short segments with approximately constant dimensions and melt flow conditions. The individual segments along each channel are then connected through nodes to their neighbors in the down- and cross-channel directions, forming a two-dimensional flow network. The process variables at each node are determined from the adjacent network element characteristics and the balance between the locally incoming and outgoing flows, which is commonly known as Kirchhoff's nodal law [28].

For modeling non-isothermal flows, the flow network consisted of two separate layers: The hydraulic network of flow rates and pressures (Figure 6) modeled the pumping behavior of each segment i by a source \dot{m}_d and conductance k in parallel, representing the local combination of drag- and pressure driven flows:

$$\dot{m} = \dot{m}_d + k [p^+ - p^-] \quad (8)$$

with \dot{m} as element flow rate, p^+ as pressure at the outflow node and p^- as pressure at the inflow node. The screw structure was discretized along the unwrapped channel length at the barrel surface, placing the nodes at the centerline of each channel. The cross-channel segments were further composed of three network elements in series, extending across the channel half-width at the pushing flight flank, the flight clearance, and the channel half-width at the trailing flight flank. Using this serial junction, the leakage flow was calculated correctly from the pressure difference between the flight flanks. Depending on the

location of the channel in the network, the mass balance reads at a particular node i [17]:

$$\begin{aligned} k_1(i-1) p_1(i-1) + [-k_1(i-1) - k_1(i) - k_b(i) - k_a(i+N_{off})] p_1(i) \\ + k_b(i) p_2(i) + k_1(i) p_1(i+1) + k_a(i+N_{off}) p_2(i-N_{off}) \\ = -\dot{m}_{d,1}(i-1) + \dot{m}_{d,1}(i) + \dot{m}_{d,b}(i) - \dot{m}_{d,a}(i+N_{off}) \end{aligned} \quad (\text{channel 1}) \quad (9)$$

$$\begin{aligned} k_a(i) p_1(i-N_{off}) + k_2(i-1) p_2(i-1) + k_b(i) p_1(i) \\ + [-k_2(i-1) - k_b(i) - k_2(i) - k_a(i)] p_2(i) + k_2(i) p_2(i+1) \\ = -\dot{m}_{d,2}(i-1) - \dot{m}_{d,b}(i) + \dot{m}_{d,2}(i) + \dot{m}_{d,a}(i) \end{aligned} \quad (\text{channel 2}) \quad (10)$$

with N_{off} denoting the offset between nodes from the same channel in the lateral direction [17]:

$$N_{off} = \text{round} \left[N_e \frac{\frac{D \pi}{\cos \varphi_b} - (w_{b,1} + w_{b,2} + e_a + e_b) \tan \varphi_b}{\frac{D \pi}{\cos \varphi_b}} \right] \quad (11)$$

depending on the pitch angle φ_b , channel widths $\{w_{b,1}, w_{b,2}\}$ and flight widths $\{e_1, e_2\}$ at the barrel, as well as the number of elements per revolution N_e .

At the inlet nodes, the channel flow rates were given by the total mass throughput \dot{m} divided by the total number of flights N_{fl} :

$$\dot{m}_{d,\{1,2\}}(1) + k_{\{1,2\}}(1) (p_{\{1,2\}}(2) - p_{\{1,2\}}(1)) = \frac{\dot{m}}{N_{fl}} \quad (12)$$

while the melt pressure and melt temperature were directly specified at the outlet nodes:

$$p_{\{1,2\}}(NN) = p_{out} \quad \text{and} \quad T_{\{1,2\}}(NN) = T_{out} \quad (13)$$

with NN as the total number of nodes in each network. Moreover, the upstream cross-channel connections were omitted for nodes

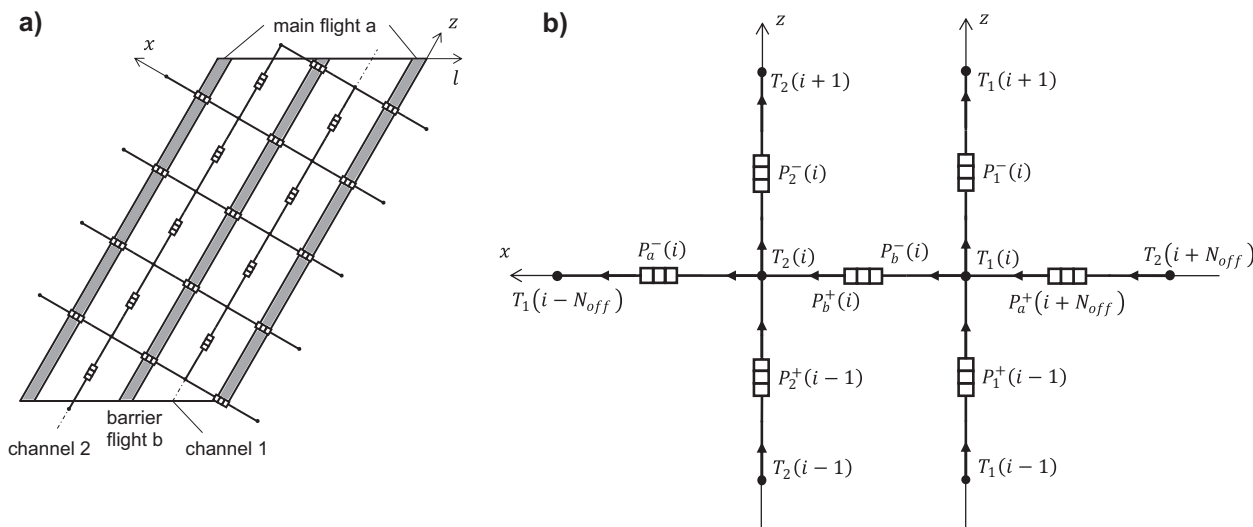


FIGURE 7 | Structure of the thermal network along a wave zone (a) and its equivalent circuit diagram (b): z ...down-channel direction, x ...cross-channel direction, l ...axial/extrusion direction.

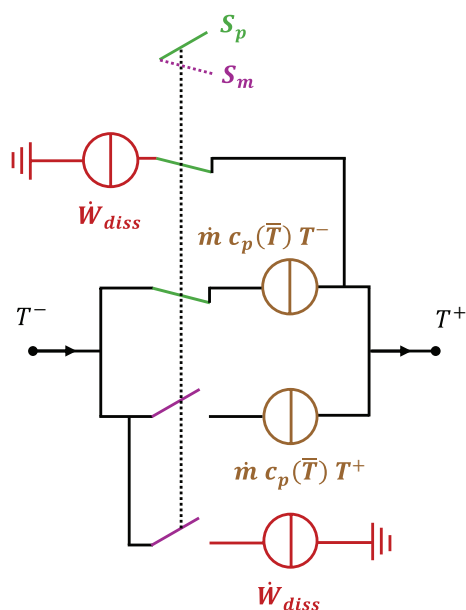


FIGURE 8 | Composition of the heater elements in the thermal network. Reproduced with permission from Roland et al. [18] 2020, Society of Plastics Engineers.

$= [1; N_{off} - 1]$, and the same applies to the downstream cross-channel connections for nodes $i = [n - N_{off} + 1; NN]$.

In the thermal network of enthalpy fluxes and temperatures (Figure 7), each segment was represented by two pairs of heat sources from convection and viscous dissipation \dot{W}_{diss} . These sources were selectively activated by a bypass valve that switches with the direction of the mass flow (Figure 8). The valve ensured that the incoming enthalpy flux and power source of each segment became effective at the outflow node. In contrast to the hydraulic network, the cross-channel segments were represented by a single thermal element associated with the convection and dissipation in the flight clearances. The arrangement of the nodes and the boundary conditions, however, coincided with the hydraulic layer for reasons of efficiency. The

thermal energy balance for both channels is then written as follows:

$$P_1^+(i-1) + P_a^+(i + N_{off}) - P_1^-(i) - P_b^-(i) = 0 \quad (\text{channel 1}) \quad (14)$$

$$P_2^+(i-1) + P_b^+(i) - P_2^-(i) - P_a^-(i) = 0 \quad (\text{channel 2}) \quad (15)$$

with the superscripts “+” and “-” referring to the positive and negative face of each heater element. The net fluxes on both sides were obtained from the following equations: [18]

$$P^- = S_p \dot{m} c_p(\bar{T}) T^- + S_m \dot{m} c_p(\bar{T}) T^+ - S_m \dot{W}_{diss} \quad (16)$$

$$P^+ = S_m \dot{m} c_p(\bar{T}) T^+ + S_p \dot{m} c_p(\bar{T}) T^- + S_p \dot{W}_{diss} \quad (17)$$

weighted by the sign functions

$$S_p = \begin{cases} 1 & \text{if } \dot{m} > 0 \\ 0.5 & \text{if } \dot{m} = 0 \\ 0 & \text{if } \dot{m} < 0 \end{cases} \quad \text{and} \quad S_m = \begin{cases} 0 & \text{if } \dot{m} > 0 \\ 0.5 & \text{if } \dot{m} = 0 \\ 1 & \text{if } \dot{m} < 0 \end{cases} \quad (18)$$

As already mentioned in Section 2.1, heat conduction was omitted in the thermal model, assuming adiabatic screw segment boundaries in all directions. This decision was motivated by two factors: First, obtaining reliable information on the actual thermal boundary conditions is challenging. The added complexity of the heat conduction modeling would have been accompanied by additional uncertainties. Second, the thermal conductance of the polymer mass can be considered low in comparison to either the heat capacitance of the flow or the viscous dissipation rate. This is evidenced by Cameron numbers below 10^{-2} or Brinkman numbers well above two, as well as by Peclét numbers far beyond one [29]. Preliminary estimations of the axial shear rate and temperature profiles indicated that this condition was fulfilled along the major portion of the melt conveying zone, even at the lowest screw speed under consideration. If necessary and sufficiently well described, the net conductive heat flux

could be superimposed on \dot{W}_{diss} as additional source term in Equations (16) and (17).

For the conventional metering zones, each node was directly connected to two nodes of the same channel across the main flight, which were located by N_{off} upstream and downstream. The corresponding nodal balance equations for this case, which are omitted here for brevity, can be found in [18].

The balance equations for the complete network eventually formed a pair of linear equations that could be solved sequentially for the nodal pressures \mathbf{p} and temperatures \mathbf{T} :

$$\mathbf{K} \mathbf{p} = \dot{\mathbf{m}} - \dot{\mathbf{m}}_d \quad (19)$$

$$\mathbf{C}_p \mathbf{T} = -\mathbf{Q} \quad (20)$$

with \mathbf{K} as conductance matrix, $\dot{\mathbf{m}}_d$ as vector of drag flows, $\dot{\mathbf{m}}$ as vector of flow boundary conditions, \mathbf{C}_p as capacitance matrix, and \mathbf{Q} as vector of heat sources and thermal boundary conditions [18].

A novel feature of this work is the concept of overlapping networks (Figure 9) to handle the transition between screw zones with a different flight number. This became relevant when simulating the two wave-type sections, as they contain short single-flighted portions at both ends. Each extruder zone was modeled by an individual two-layer network, which was extended by an inlet over two revolutions and an outlet over one revolution using the dimensions at the original boundary nodes. The average pressures and temperatures were then calculated across the extended zone lengths and aligned at the actual axial positions of the zone interfaces. With these virtual extensions, each network element along the actual zone length was always connected to four neighbors, which avoided numerical artifacts and stabilized the computation. The values along the inlet and outlet sections were eventually omitted for all post-processing operations.

3.2 | Local Melt Conveying Characteristics

The local pumping characteristics and viscous dissipation rate of each network element were described by three sets of analytical

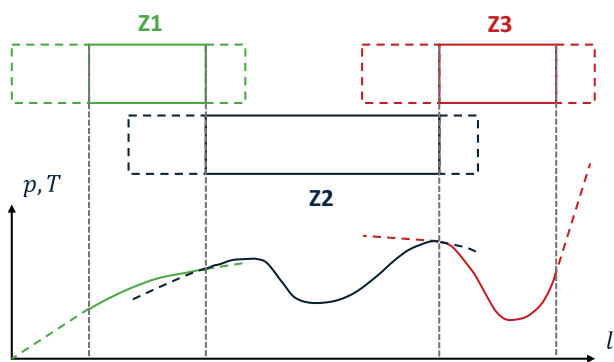


FIGURE 9 | Concept of overlapping networks for multiple differently flighted extruder zones (dashed lines: Virtual zone extensions, solid lines: Final prediction).

equations referring to (i) three-dimensional curved channel flow, (ii) two-dimensional curved channel flow, and (iii) two-dimensional leakage flow of a power-law fluid. These advanced models replaced the previously employed straight channel models [30–32], the Newtonian representative shear rate model [7, 33] and the Newtonian leakage flow models [7, 33] to gain prediction accuracy for high-performance metering screws with deep channels, flight undercuts, and strongly overridden sections. To capture the mathematically complex flow situation by condensed and generally valid functions, we had adopted a hybrid modeling strategy outlined in [34] that effectively combines analytical, numerical, and data-driven techniques: First, the governing equations had been formulated for each local flow problem in dimensionless form. The scaled flow equations had then been solved numerically for a wide range of parameter combinations for both conventional and high-performance extrusion conditions. Finally, symbolic regression using genetic programming had been performed on the numerical database to derive continuous analytical functions. These functions express the mathematical dependencies of

- the dimensionless flow rate Π_V and dimensionless dissipation rate Π_Q in the channel,
- the dimensionless flow rate Π_V^δ and dimensionless dissipation rate Π_Q^δ in the flight gap,
- and the dimensionless volumetrically averaged shear rate Π_S in the channel


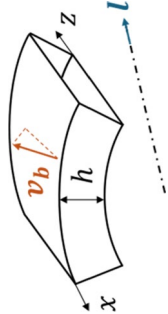
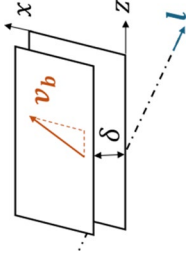
as functions of the following independent dimensionless parameters:

- the channel depth ratio h/D
- the screw pitch ratio t/D ,
- the channel aspect ratio h/w_b (3D case only),
- the power-law exponent n ,
- the dimensionless down-channel pressure gradient $\Pi_{p,z}$ or the dimensionless flow rate Π_V ,
- and the dimensionless cross-channel pressure gradient $\Pi_{p,x}^\delta$ or the dimensionless leakage flow rate Π_V^δ .

Table 7 summarizes the physical assumptions and related variables of the advanced melt conveying models, and Table 8 provides the ranges of validity of the advanced models compared to their originally implemented predecessors. The equations for the two-dimensional curved channel models, which are based on the simulations by Roland et al. [36] and have not been published before, are additionally provided in Section S1 alongside this article. For detailed information on the model development, the reader is referred to the articles cited in the table. The data-based modeling step for the 2D curved channel models will be further disclosed in an upcoming publication.

Four supplementary steps were executed to determine representative network element properties from the regression models. First, the effect of the flight undercuts on the channel flow was approximately considered by a weighted average between the two- and three-dimensional channel models:

TABLE 7 | Overview of the advanced local melt conveying models used within the network-theory-based calculation.

	3D curved channel [35]	2D curved channel [36]	2D leakage [37], [data 5]
Kinematic model			
Modeled dependencies	<p>ω...screw speed, l...axial coordinate, x...cross-channel coordinate, z...down-channel coordinate, v_b...relative rotational velocity of the barrel</p> $\Pi_V \left(\frac{h}{D}, \frac{t}{D}, \frac{h}{w_b}, n, \Pi_{p,z} \right)$ $\Pi_Q \left(\frac{h}{D}, \frac{t}{D}, \frac{h}{w_b}, n, \Pi_V \right)$ $\Pi_S \left(\frac{h}{D}, \frac{t}{D}, \frac{h}{w_b}, n, \Pi_V \right)$	$\Pi_V \left(\frac{h}{D}, \frac{t}{D}, n, \Pi_{p,z} \right)$ $\Pi_Q \left(\frac{h}{D}, \frac{t}{D}, n, \Pi_V \right)$	$\Pi_V^\delta \left(\frac{t}{D}, n, \Pi_{p,x}^\delta \right)$ $\Pi_Q^\delta \left(\frac{t}{D}, n, \Pi_V^\delta \right)$
Assumptions on the flow	<ul style="list-style-type: none"> • Isothermal • Fully developed • Negligible mass forces (creeping flow) • Incompressible, inelastic power-law fluid • Wall adhesion • Zero cross-channel flow rate • Full flight effect 	<ul style="list-style-type: none"> • Isothermal • Fully developed • Negligible mass forces (creeping flow) • Incompressible, inelastic power-law fluid • Wall adhesion • Zero cross-channel flow rate • No flight effect 	<ul style="list-style-type: none"> • Isothermal • Fully developed • Negligible mass forces (creeping flow) • Incompressible, inelastic power-law fluid • Wall adhesion • Zero down-channel pressure gradient • No flight effect

Note: The subfigure for the 2D curved channel has been reproduced with permission from Roland et al. [36] 2018, Society of Plastics Engineers. The subfigure for the 2D leakage gap has been reproduced under the terms of the CC-BY license [37]. 2021, Marschik et al., published by MDPI.

TABLE 8 | Ranges of validity of the advanced melt conveying characteristics compared to their predecessor models used in [17, 18].

Pumping/dissipation, 2D/3D channel flow		Shear rate, channel flow		Leakage flow	
Marschik et al. [30]/ Roland et al. [32]/ Roland et al. [31]	Present	Mohr, Mallouk [7]/Giesekus et al. [33]	Present	Mohr, Mallouk [7]/Giesekus et al. [33]	Present
$h/D \ll 0.1$	$0.025 \leq h/D \leq 0.325$	$h/D \ll 0.1$	$0.025 \leq h/D \leq 0.325$	$\delta/D \ll 0.1$	$\delta/D \ll 0.1$
$0.5 \leq t/D \leq 2.0$	$0.6 \leq t/D \leq 2.4$	$t/D > 0$	$0.6 \leq t/D \leq 2.4$	$t/D > 0$	$0.5 \leq t/D \leq 2.47$
$h/w_b \leq 0.5$	$h/w_b \leq 1.3$	$h/w_b \ll 0.1$	$h/w_b \leq 1.3$	$n = 1.0$ (Newtonian)	$0.2 \leq n \leq 1.0$
$0.2 \leq n \leq 1.0$	$0.2 \leq n \leq 1.0$	$n = 1.0$ (Newtonian)	$0.2 \leq n \leq 1.0$		$-2000 \leq \Pi_V^\delta \leq 2000$
$0 < \Pi_V < 3.0$	$\Pi_{p,z} \geq -1.1$ $\Pi_V > 0$		$\Pi_{p,z} \geq -1.1$ $\Pi_V > 0$		

Note: The bold values refer to the extended application ranges of our advanced local melt conveying characteristics - a key aspect that qualifies the network analysis approach for evaluating high-performance screws.

$$\begin{pmatrix} \Pi_V \\ \Pi_Q \\ \Pi_S \end{pmatrix} = \frac{\delta_a + \delta_p}{2h} \begin{pmatrix} \Pi_{V,2D} \\ \Pi_{Q,2D} \\ \Pi_{S,3D}(h/w_b=0) \end{pmatrix} + \left(1 - \frac{\delta_a + \delta_p}{2h}\right) \begin{pmatrix} \Pi_{V,3D} \\ \Pi_{Q,3D} \\ \Pi_{S,3D} \end{pmatrix} \quad (21)$$

with δ_a and δ_p denoting the clearances at the active and passive flight flank, respectively. The weighting of the shear rate was performed by extrapolating the three-dimensional model to zero aspect ratio, as no distinct two-dimensional curved-channel model was available. Second, local power-law parameters were derived from the more descriptive Carreau-Yasuda model for each element to capture the rheological behavior of the melt. They were obtained from the slope and intercept of the tangent on the viscosity curve at the element shear rate in a double-logarithmic scale according to: [16]

$$n = 1 + \frac{(\eta_0 - \eta_\infty) \cdot (n_{CY} - 1) \cdot (a_T \cdot \lambda \cdot \dot{\gamma})^a \cdot (1 + (a_T \cdot \lambda \cdot \dot{\gamma})^a)^{\frac{n_{CY}-1-a}{a}}}{\eta_\infty + (\eta_0 - \eta_\infty) \cdot (1 + (a_T \cdot \lambda \cdot \dot{\gamma})^a)^{\frac{n_{CY}-1}{a}}}, \quad (22)$$

$$K = a_T \left[\eta_\infty + (\eta_0 - \eta_\infty) \cdot (1 + (a_T \cdot \lambda \cdot \dot{\gamma})^a)^{\frac{n_{CY}-1}{a}} \right] \dot{\gamma}^{1-n}, \quad (23)$$

corrected by the pre-factor a_T for K to match the definition of the power-law within the local melt conveying models. The shear rates $\dot{\gamma}$ in the screw channel segments were given by the dimensional form of the weighted shear rates Π_S ,

$$\dot{\gamma} = \frac{v_{b,z}}{h} \Pi_S \quad (24)$$

while the shear rates in the flight clearance segments $\dot{\gamma}^\delta$ were estimated from a Newtonian pumping model [7] to

$$\dot{\gamma}^\delta = \frac{v_{b,x}}{\delta} \sqrt{[1 + 3 e(n) (\Pi_V^\delta - 1)]^2 + \left[\frac{\pi}{t/D}\right]^2} \quad (25)$$

at a dimensionless radial position

$$e(n) = \begin{cases} \exp(-1/3) & \text{if } n = 1 \\ \left(\frac{3n}{2n+1}\right)^{\frac{n}{1-n}} & \text{otherwise} \end{cases} \quad (26)$$

proposed by Giesekus et al. [33] Third, describing the pumping behavior by source-conductance elements required the nonlinear pressure-throughput relationships to be linearized at the local operating point. Due to the complexity of the equations, this linearization was performed numerically by computing the difference quotient across a small positive shift of 10^{-3} in the dimensionless pressure gradient.

Finally, as extension to the original framework of Roland et al. [18], the temperature variation across the flights was considered for calculating the dissipation rates in the clearances. To this end, the isothermal dissipation rate was corrected by a thermal energy balance based on the analytical solutions (7.386–7.387) by Rauwendaal [38] for the adiabatic temperature rise of a uni-directional flow of power-law fluids:

$$\dot{W}_{diss}^\delta = \frac{|\dot{m}^\delta| c_p(\bar{T})}{\beta_{loc}} \ln \left[1 + \frac{\beta_{loc} \dot{W}_{diss,iso}^\delta}{|\dot{m}^\delta| c_p(\bar{T})} \right] \quad (27)$$

The temperature sensitivity coefficient for the local power-law model β_{pl} was determined from the ratio of consistencies after perturbing the local average melt temperature by $+1^\circ\text{C}$:

$$\beta_{loc} = \ln \left(\frac{K(\bar{T})}{K(\bar{T} + 1)} \right) \quad (28)$$

The dissipation model in the flight clearance further needed to be numerically stabilized to avoid singularities occurring with the version of Marschik et al. [37] by truncating the denominators to a minimum absolute value of 10^{-6} . The stabilized version was uploaded on the public repository Zenodo^[data5] and is strongly advised for any future evaluations.

3.3 | Simulation Procedure

The calculation routine was executed within the academic programming environment of MATLAB 2022b (MathWorks Inc.), following the flowchart outlined in Figure 10. First, the necessary inputs for the calculation were defined, comprising (i) the material model parameters, (ii) the screw and barrel structures, the (iii) screw speed, (iv) throughput, (v) back pressure, and (vi) outlet melt temperature as process parameters, and (vi) the settings for the numerical solution algorithm (models and solver parameters). Next, the flow network was

built by discretizing each extruder zone with 150 elements per revolution, adding the virtual inlet and outlets, and interpolating the extruder dimensions at the nodal points. The numerical calculation was then initialized by reading the coefficients of the regression models, setting the nodal pressures and element flow rates to zero, and assigning the melt temperature at the screw tip to the temperature nodes. From this point onwards, eight successive steps were executed iteratively:

1. Obtain the hydraulic element characteristics from the average nodal variables and the models for the density, viscosity,

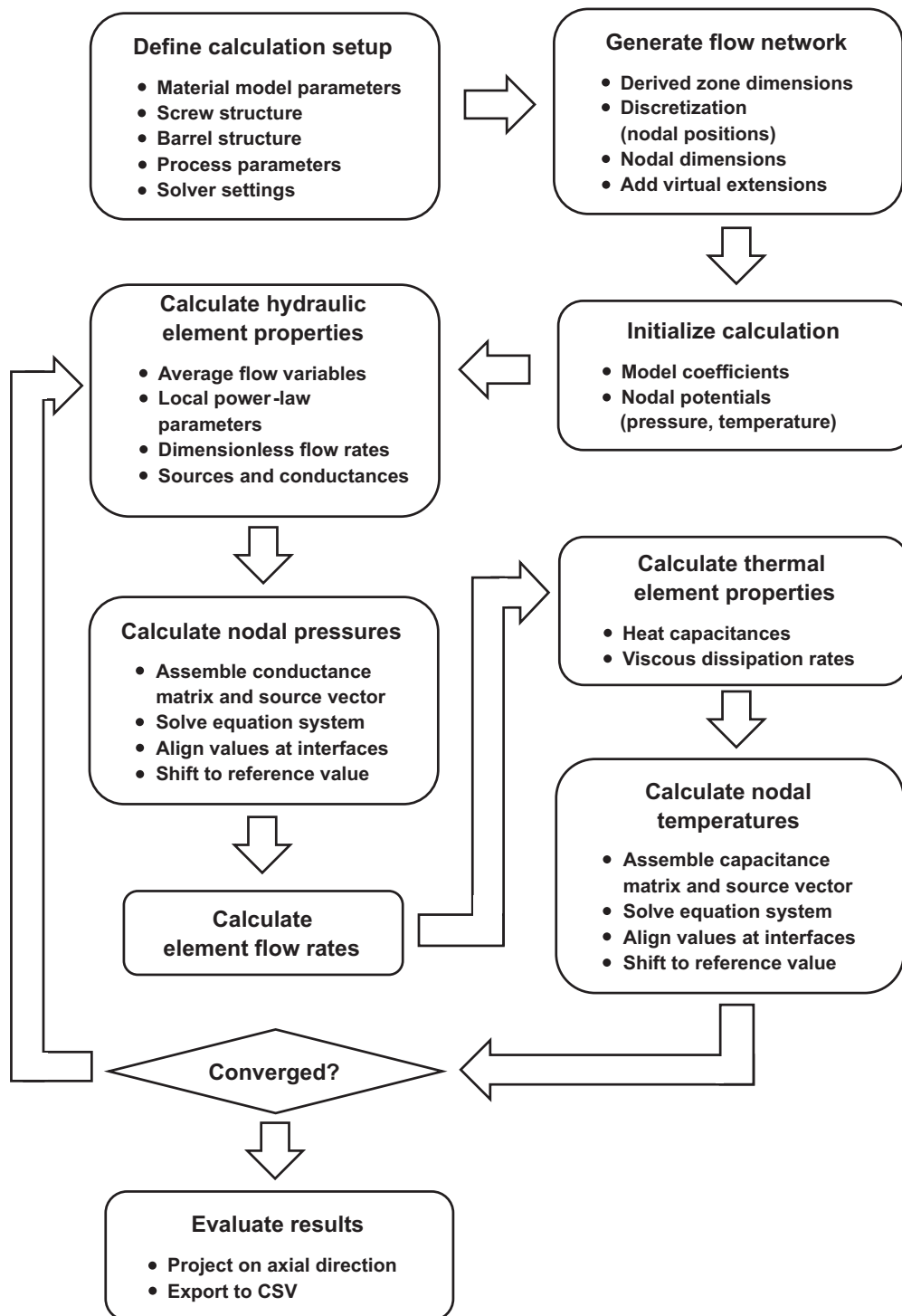


FIGURE 10 | Flowchart of the network-theory-based extruder calculation.

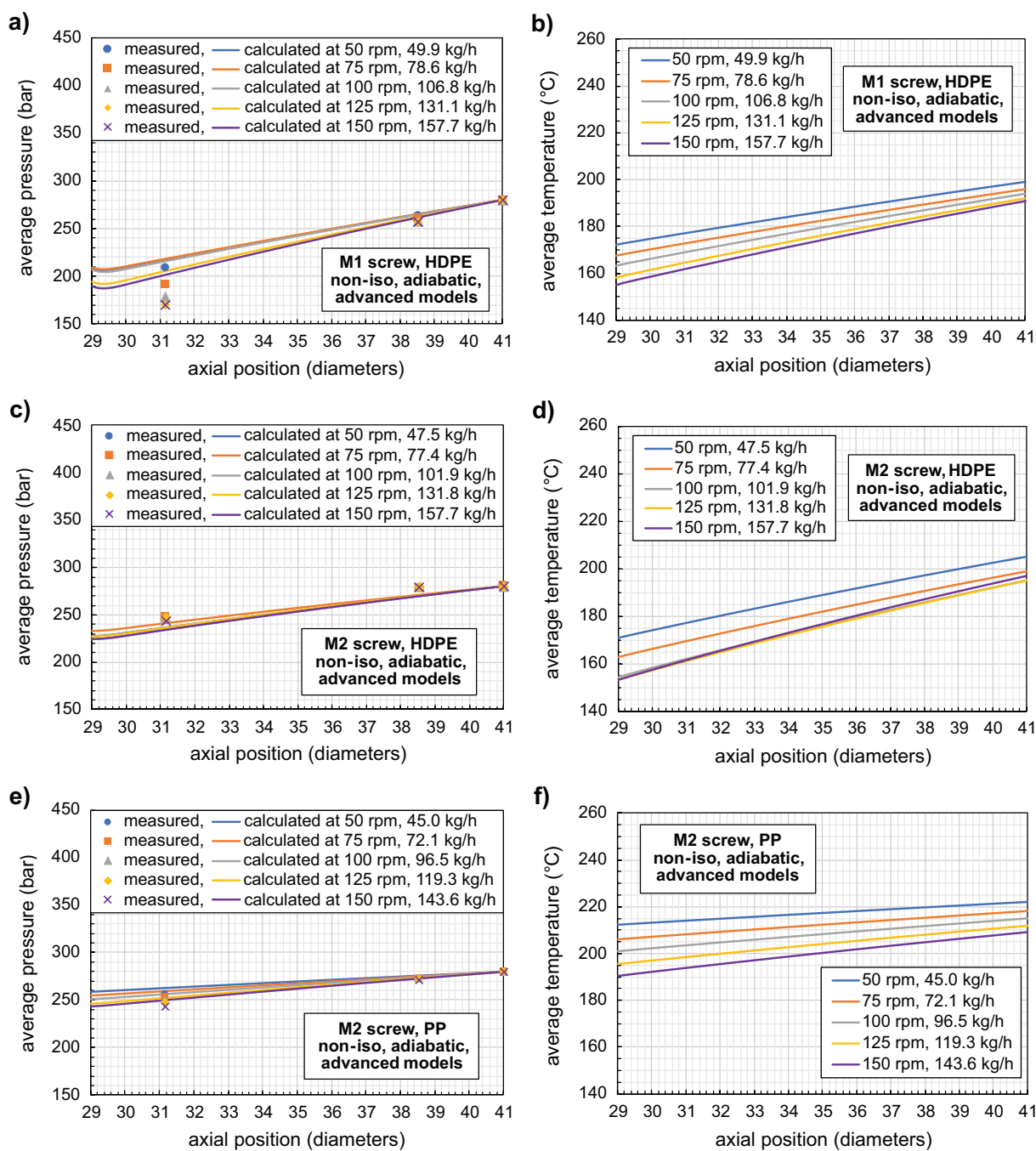


FIGURE 11 | Measured average pressures (symbols), calculated average pressures, and calculated average temperatures (curves) along the metering zone for the HDPE grade and screw M1 (a, b), the HDPE grade and screw M2 (c, d), and the PP grade and screw M2 (e, f).

dimensionless flow rate and dimensionless shear rate. The shear rate models and viscosity curve tangents were alternately evaluated in an inner iteration loop to determine the local power-law parameters, starting from the case of simple shear ($\Pi_s = 1$).

2. Assemble the equation system for the mass balance and solve it for the nodal pressures.
3. Align the pressures at the zone interfaces and shift the complete pressure profile to the reference value at the screw tip.

4. Evaluate the element flow rates from the pressure profile.
5. Determine the thermal element characteristics from the average segment variables, using the models for the specific heat capacity and dimensionless dissipation rate.
6. Assemble the equation system for the thermal power balance and solve it for the nodal temperatures.
7. Align the temperatures at the zone interfaces and shift the complete temperature profile to the reference value at the screw tip.

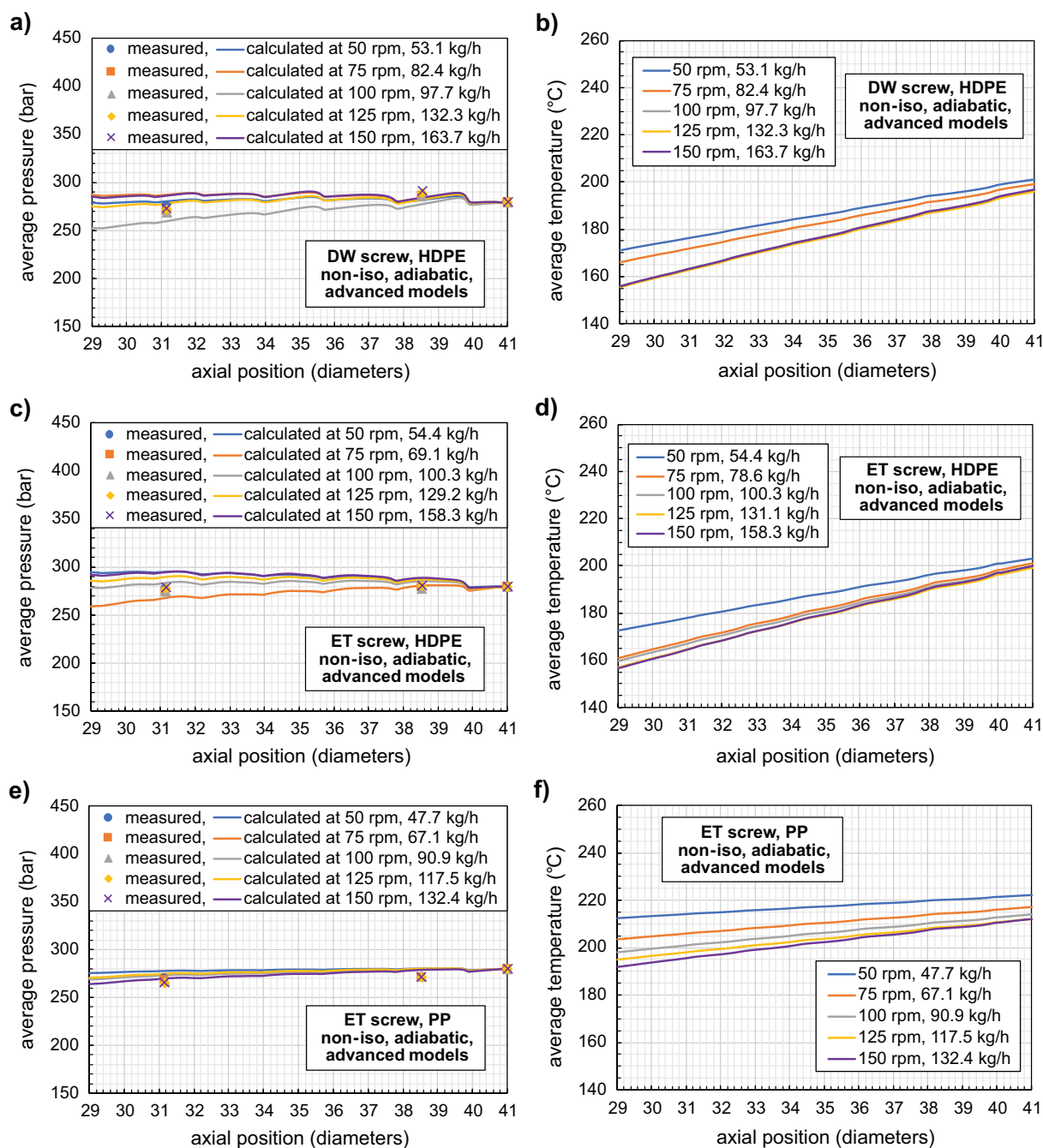


FIGURE 12 | Measured average pressures (symbols), calculated average pressures, and calculated average temperatures (curves) along the wavy-metering zones for various extrusion setups.

8. Check for convergence and resort to step 1 if necessary.

The calculation was considered converged once the total pressure and temperature difference across the entire metering zone had changed by less than 1% in the current iteration or after 10 iterations had been completed. In all cases, convergence was reached before this hard limit. Finally, the nodal values were projected on the extruder axis to facilitate comparison with the experiments, and subsequently exported as comma-separated values.

4 | Results and Discussion

4.1 | Deep-Flighted Metering Zones

Figure 11 displays the measured and calculated average pressures and temperatures for three setups involving the deep-flighted metering screws: the high-viscous HDPE grade alongside the ultra-deep screw M1 (a, b) and the high-pitch screw M2 (c, d), as well as the low-viscous PP grade alongside the high-pitch screw M2. In all cases, the metering zones generated pressure along the screw length except for a small piece

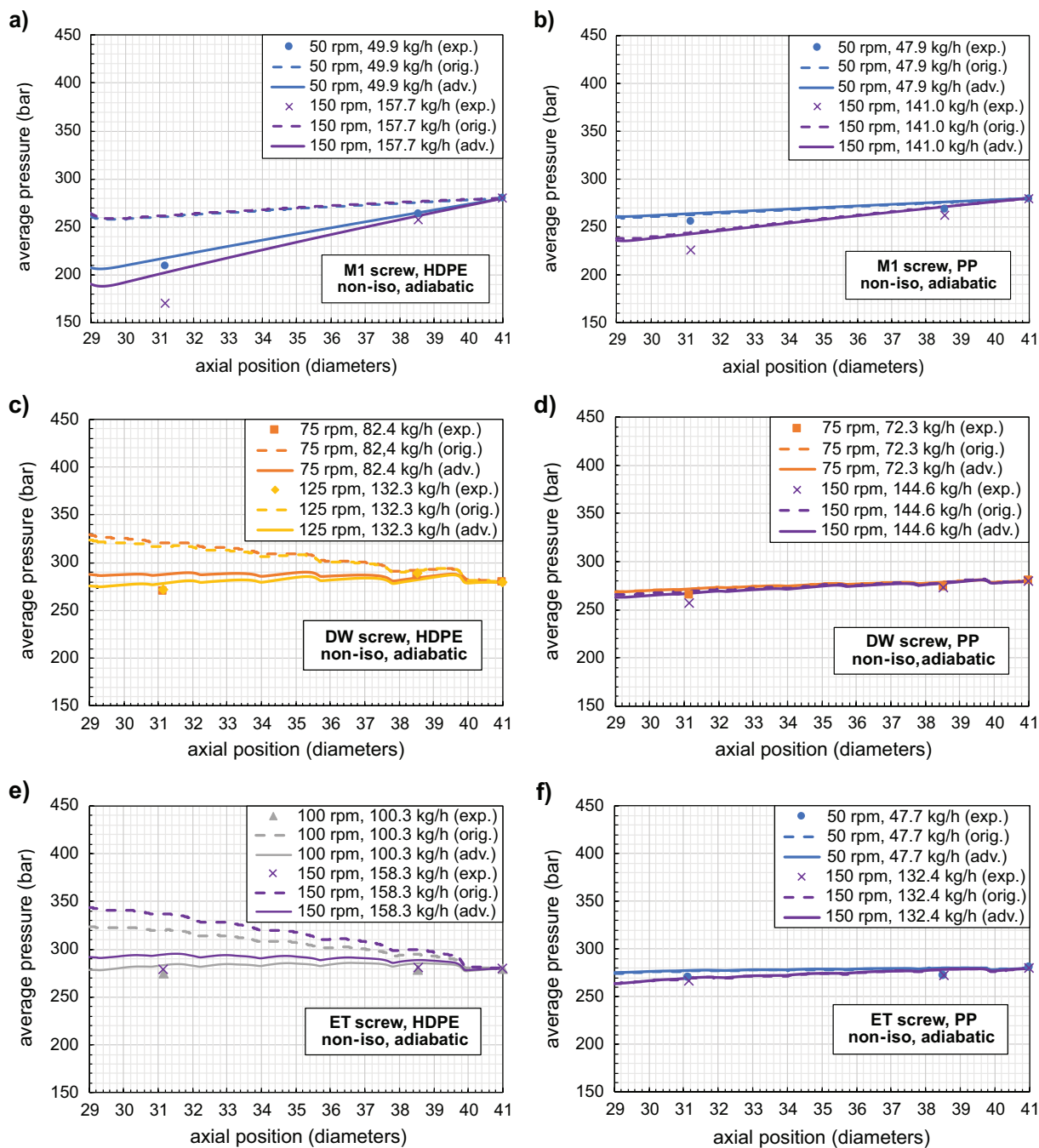


FIGURE 13 | Measured average pressures (symbols) compared to the calculated average pressures using the advanced models (solid curves) and original models (dashed curves) for selected extrusion setups.

at the inlet, which can be attributed to the large drag flow capacity of the screws. The pressure rise was steeper for screw M1 due to its lower pitch, causing larger back-flow resistance through longer down-channel distance per revolution and less pronounced cross-channel flow. The pressure buildup was substantially lower for the less viscous PP as expected, while the screw speed affected the pressure profiles only slightly. The melt temperatures, on the other hand, consecutively dropped with higher screw speeds except for the HDPE and screw M2 between 125 and 150 rpm. This indicates that the melt temperature was largely governed by less effective plastication in the upstream barrier zone, which became overruled by increased viscous dissipation in the exceptional case. The effect of viscous dissipation

is reflected in the increasing slope of the temperature curves at higher screw speeds, for the higher viscous material, and for the high-pitch screw M2 with enhanced transverse flow.

All in all, the calculated profiles follow the expected trends and are in good agreement with the measured values. Merely for the HDPE and screw M1, the rearmost pressure P6 was distinctly overpredicted for all operating points. The systematic deviation can be linked to two missing features of the calculation: First, the calculations were based on viscosity data at or close to atmospheric pressures. When pressurized to 150–300 bar in the extruder, the melt viscosity can be 10%–20% higher compared to the rheological measurements, depending on the value of the

pressure-sensitivity coefficient [39]. The pressure-induced viscosity increase is reflected by higher pressure gradients in the experiments. Second, the calculations assumed a homogeneous polymer melt throughout the entire zone length. However, streaks in the extrudate had already been visible during the experiments at 150 rpm, suggesting incomplete melting. Therefore, it is likely that residual solid particles existed at the beginning of the melt conveying zone also at lower speeds, contributing to locally increased viscosities and pressure gradients within this section. Difficulties in melting would further explain why the predictions became less accurate at higher throughputs. As both phenomena primarily influenced the conductance of the screw channel, they became less significant for lower average pressure gradients, which explains the better corresponding results in the other two cases.

4.2 | Wave-Type Metering Zones

The average pressure and temperature development in the wave-type metering zones is presented in Figure 12: Experimental and simulative results are compared for the DW and ET zone processing the high-viscous HDPE, and for the ET zone conveying the more easily flowable PP. As indicated by the measurements, both wave screws operated under nearly pressure-neutral conditions, with a slightly superior pumping capability achieved by the DW design. These findings are in accordance with previous observations and were also captured by the simulations: For all setups, the simulated pressure profiles closely matched the experimental data. The single curves departing from the remaining graphs in charts (a) and (c) were probably caused by slight errors in the measured throughput (the respective specific outputs were exceptionally low). The pressure and temperature profiles further exhibit six wave-like oscillations associated with the cyclic variation of the channel depth. These initially weak oscillations grow in amplitude toward the screw tip as the compression ratio of the waves becomes larger (Figure 5). Moreover, the local pressure and temperature gradients were much smoother for the low-viscous PP. With reduced pressure gradients, weaker cross-channel flows and thus inferior mixing action are expected compared to the high-viscous melt. In case of low-viscous polymers, lower pitches or steeper compression of the waves are therefore advisable to counteract the reduced mixing. On average, the trends for the melt temperature are similar to the metering zones, caused by the competing effects of delayed upstream plastification and increased dissipation.

4.3 | Impact of the Advanced Melt Conveying Models

Elevating the network-based approach to the present level of sophistication required substantial efforts for developing the new regression models. To assess the usefulness of these advanced models, we additionally evaluated our calculation tool with the melt-conveying models originally employed in [17, 18], which assume a flat channel and a Newtonian representative viscosity in the flight gaps. Figure 13 compares the predicted pressure profiles of both program versions with the measured values for selected extrusion conditions. In case of the highly viscous and

strongly shear-thinning HDPE, the original models departed significantly more extremely from the experiments. As this also applied to the M1 and DW design with small leakage gaps, the inferior predictions can be largely attributed to the neglected curvature of the channel: The flat-plate approximation is known to systematically underestimate the pumping capability of deep channels for low power-law indices and practically relevant dimensionless pressure gradients, which is reflected in the results. For the setups involving the less viscous, less shear-thinning PP, both model versions performed at a roughly similar level. Apparently, the net effect of channel curvature was small for the parameter combinations for this material, which was probably caused by the compensating effects of stress concentration and reduced flow-through area [35]. The overall prediction accuracy, however, improved considerably when choosing the advanced models, which confirms their added value for analyzing high-performance metering zones.

5 | Conclusions

An advanced fast-computing routine based on network theory was employed to investigate the pumping capability and melt temperature development of high-performance metering sections in single-screw extrusion. Unlike previously published versions, this new routine features more generally valid regression models that capture the effects of channel curvature and undercut flights, which are particularly relevant for wave-dispersion screws. In addition, the non-isothermal melt conveying behavior can now be predicted for arbitrary junctions of conventional and wave-type metering zones. The calculation tool was applied to distinct experimental setups on a high-speed extruder involving smooth deep-flighted designs, a double-wave design, and an energy-transfer design in the metering zone, as well as two rheologically different polymers. In all cases, the calculated pressures were in good accordance with the experimentally measured values. Furthermore, the effects of screw pitch and melt viscosity on the pressure and temperature profiles were correctly represented. Even for the setups with the largest deviations, the predictions of the advanced framework were substantially more accurate than its equivalent based on the flat plate approximation, demonstrating the beneficial impact of the curved channel models. The calculations further provided valuable insights into the melt conveying behavior of wave-dispersion screws: For instance, the double-wave design achieved superior pumping capability compared to the energy-transfer design with the same channel profile. Moreover, the wave-like pressure and temperature oscillations were weaker for the lower viscous material, suggesting a more restrictive channel profile for improved mixing.

Despite the convincing predictive capabilities, the modeling approach still leaves space for improvement. Considering heat transfer from the barrel and the influence of pressure on viscosity would describe the melt conveying conditions more realistically, especially for high-viscous polymers. As a pure flow simulation approach, the model further becomes less reliable for the plastifying part of the extruder, where solid and molten polymer coexist. Integrating solids conveying and melting models into the calculation would enable a holistic analysis of the extruder and hence significantly boost its practical utility. Aside from further

modeling efforts, we would like to validate the calculation routine against a wider range of screw designs and materials (such as barrier screws and amorphous polymer grades), additionally addressing the power consumption along the metering zone. A patented laser beam deflection technique [40] could provide experimental benchmarks for the drive power calculation.

Notwithstanding the various routes for future research, the advanced network analysis tool already offers an appealing option for designing and troubleshooting high-performance single-screw extruders. Since reasonably accurate pressure and temperature profiles are predicted within a few minutes, this calculation tool can significantly accelerate decision-making. This further contributes to shorter development cycles and downtimes, paving the way for more efficient and eco-friendly extrusion of polymers.

Acknowledgments

Special credits go to Erwin Krenner, Hannah Zeilinger, and Katharina Weingartshofer for their valuable support during the experiments. Many thanks are also devoted to Maximilian Zacher for transferring the network-based calculation into a user-friendly computational tool. The authors further express their gratitude to the project partners from the University of Paderborn under the lead of Prof. Volker Schöppner for characterizing the physical properties of the HDPE pipe grade. Open Access funding provided by Johannes Kepler Universität Linz/KEMÖ.

Funding

This work was supported by the Austrian Science Fund (Grant-DOIs: 10.55776/I4872 and 10.55776/PIN4613324), and the COMET Center CHASE, Austrian Research Promotion Agency (FFG).

Conflicts of Interest

The authors declare no conflicts of interest.

Data Availability Statement

The data supporting the findings of the study are available on the public repository Zenodo by accessing the persistent identifiers stated below. This includes

- [data1, data2] the material data of the polymer grades (<https://doi.org/10.5281/zenodo.17672065>; <https://doi.org/10.5281/zenodo.17672111>).
- [data3] the structural data of the screw extensions (<https://doi.org/10.5281/zenodo.17673742>).
- [data4] the experimental data from the throughput tests (<https://doi.org/10.5281/zenodo.17672241>).
- [data5] the stabilized model for the viscous dissipation in the flight clearance (<https://doi.org/10.5281/zenodo.17403837>).
- and [data6] the simulation results from the network analysis (<https://doi.org/10.5281/zenodo.18805116>).

Other kinds of data are available on request from the authors.

References

1. G. A. Kruder, "Extrusion Apparatus and Method," United States Patent 4173417, 1979.
2. C. I. Chung and R. A. Barr, "Energy Efficient Extruder Screw," United States Patent 4405239, 1983.

3. H. S. Rowell and D. Finlayson, "Screw Viscosity Pumps," *Engineering* 114 (1922): 606–607.
4. H. S. Rowell and D. Finlayson, "Screw Viscosity Pumps," *Engineering* 126 (1928): 249–250.
5. M. L. Booy, "Influence of Channel Curvature on Flow, Pressure Distribution, and Power Requirements of Screw Pumps and Melt Extruders," *Polymer Engineering and Science* 3, no. 3 (1963): 176–185, <https://doi.org/10.1002/pen.760030305>.
6. J. F. Carley, R. S. Mallouk, and J. M. McKelvey, "Simplified Flow Theory for Screw Extruders," *Industrial and Engineering Chemistry* 45, no. 5 (1953): 974–978, <https://doi.org/10.1021/ie50521a032>.
7. W. D. Mohr and R. S. Mallouk, "Flow, Power Requirement, and Pressure Distribution of Fluid in a Screw Extruder," *Industrial and Engineering Chemistry* 51, no. 6 (1959): 765–770, <https://doi.org/10.1021/ie50594a034>.
8. K. H. Lim, W. R. Hwang, and S. J. Kim, "A Finite-Element Technique for Flows in the Single Screw Extruder Using a Partial Periodic Unit," *Korea-Australia Rheology Journal* 31, no. 1 (2019): 59–67, <https://doi.org/10.1007/s13367-019-0007-4>.
9. M. Ghoreishy, M. Razavi-Nouri, and G. Naderi, "Finite Element Analysis of a Thermoplastic Elastomer Melt Flow in the Metering Region of a Single Screw Extruder," *Computational Materials Science* 34, no. 4 (2005): 389–396, <https://doi.org/10.1016/j.commatsci.2005.01.011>.
10. T. A. Plumley, M. A. Spalding, J. Dooley, et al., "Three-Dimensional Numerical Analysis of an Energy Transfer (ET) Screw Section of a Single-Screw Extruder," in *Proceedings of the 52nd Annual Technical Conference of the Society of Plastics Engineers (SPE ANTEC)* (Society of Plastics Engineers, 1994).
11. J. Perdikoulis, J. Svabik, and T. Womer, "3D FEM Analysis of a Wave Type Screw Channel," in *Proceedings of the 67th Annual Technical Conference of the Society of Plastics Engineers (SPE ANTEC)*, vol. 2 (Society of Plastics Engineers, 2009), 1180–1187.
12. M. Dörner, "Wave-Schnecken in der Einschneckenextrusion," PhD thesis, Paderborn University, 2022.
13. H. Potente, W. Hanhart, and T. Reski, "Design and Processing Optimization of Extruder Screws," *Polymer Engineering and Science* 34, no. 11 (1994): 937–945, <https://doi.org/10.1002/pen.760341111>.
14. A. R. Vincelette, C. S. Guerrero, P. J. Carreau, and P. G. Lafleur, "A Model for Single-Screw Plasticating Extruders," *International Polymer Processing* 4, no. 4 (1989): 232–241, <https://doi.org/10.3139/217.890232>.
15. K. Wilczyński, "Single-Screw Extrusion Model for Plasticating Extruders," *Polymer-Plastics Technology and Engineering* 38, no. 4 (1999): 581–608, <https://doi.org/10.1080/03602559909351602>.
16. C. Marschik, W. Roland, and J. Miethlinger, "A Network-Theory-Based Comparative Study of Melt-Conveying Models in Single-Screw Extrusion: A. Isothermal Flow," *Polymers* 10, no. 8 (2018): 929–940, <https://doi.org/10.3390/polym10080929>.
17. C. Marschik, W. Roland, M. Dörner, et al., "Application of Network Analysis to Flow Systems With Alternating Wave Channels: Part B. (Superimposed Drag-Pressure Flows in Extrusion)," *Polymers* 12, no. 9 (2020): 1900–1923, <https://doi.org/10.3390/polym12091900>.
18. W. Roland, C. Marschik, A. Hammer, et al., "Modeling the Non-Isothermal Conveying Characteristics in Single Screw Extrusion by Application of Network Analysis," in *Proceedings of the 78th Annual Technical Conference of the Society of Plastics Engineers (SPE ANTEC)*, vol. 1 (Society of Plastics Engineers, 2020), 388–395.
19. M. Zacher, "A Network-Theory-Based Approach Modeling Barrier Screws in Combination with Grooved Plasticizing Barrels," PhD thesis, Johannes Kepler University Linz, 2023.
20. B. Rabinowitsch, "Über die Viskosität und Elastizität von Solen," *Zeitschrift für Physikalische Chemie* 145A, no. 1 (1929): 1–26, <https://doi.org/10.1515/zpch-1929-14502>.

21. W. P. Cox and E. H. Merz, "Correlation of Dynamic and Steady Flow Viscosities," *Journal of Polymer Science* 28, no. 118 (1958): 619–622, <https://doi.org/10.1002/pol.1958.1202811812>.
22. K. Yasuda, R. C. Armstrong, and R. E. Cohen, "Shear Flow Properties of Concentrated Solutions of Linear and Star Branched Polystyrenes," *Rheologica Acta* 20 (1981): 163–178, <https://doi.org/10.1007/BF01513059>.
23. G. Menges, F. Wortberg, and W. Michaeli, "Estimating the Viscosity Function via the Melt Flow Index," *Kunststoffe/Plastics Insights* 68 (1978): 47–50.
24. P. G. Tait, "Report on Some of the Physical Properties of Fresh Water and of Sea Water," in *Report on the Scientific Results of the Voyage of the H.M.S. Challenger During the Years 1873–76: Physics and Chemistry*, ed. J. Murray, C. W. Thomson, G. S. Nares, et al. (Her Majesty's Stationery Office, 1884).
25. International Organization for Standardization, "Plastics: Differential Scanning Calorimetry (DSC)," ISO 11357-1:2023, 2023.
26. A. Hammer, "Analyse von schnellaufenden High-Performance Schnecken für die Extrusion von hochmolekularen Polyolefinen (mittels Nutbuchsenextruder)," Master's Thesis, Johannes Kepler University Linz, 2018.
27. H. Hörmann, "Theoretische und experimentelle Betrachtung schnelllaufender Einschnckenextruder," PhD thesis, Paderborn University, 2014.
28. G. R. Kirchhoff, "Ueber den Durchgang eines elektrischen Stromes durch eine Ebene, insbesondere durch eine kreisförmige," *Annalen der Physik Und Chemie* 64 (1845): 497–514, <https://doi.org/10.1002/andp.18451400402>.
29. J.-F. Agassant, *Polymer Processing: Principles and Modeling*, 2nd ed. (Hanser, 2017).
30. C. Marschik, W. Roland, B. Löw-Baselli, and J. Miethlinger, "A Heuristic Method for Modeling Three-Dimensional Non-Newtonian Flows of Polymer Melts in Single-Screw Extruders," *Journal of Non-Newtonian Fluid Mechanics* 248 (2017): 27–39, <https://doi.org/10.1016/j.jnnfm.2017.08.007>.
31. W. Roland, M. Kommenda, C. Marschik, et al., "Extended Regression Models for Predicting the Pumping Capability and Viscous Dissipation of Two-Dimensional Flows in Single-Screw Extrusion," *Polymers* 11, no. 2 (2019): 334–369, <https://doi.org/10.3390/polym11020334>.
32. W. Roland, C. Marschik, M. Krieger, B. Löw-Baselli, and J. Miethlinger, "Symbolic Regression Models for Predicting Viscous Dissipation of Three-Dimensional Non-Newtonian Flows in Single-Screw Extruders," *Journal of Non-Newtonian Fluid Mechanics* 268 (2019): 12–29, <https://doi.org/10.1016/j.jnnfm.2019.04.006>.
33. H. Giesekus and G. Langer, "Die Bestimmung der wahren Fließkurven nicht-newtonscher Flüssigkeiten und plastischer Stoffe mit der Methode der repräsentativen Viskosität," *Rheologica Acta* 16 (1977): 1–22, <https://doi.org/10.1007/BF01516925>.
34. W. Roland, M. Kommenda, and G. Berger-Weber, "Application of Symbolic Regression in Polymer Processing," in *Proceedings of the 24th International Symposium on Symbolic and Numeric Algorithms for Scientific Computing (SYNASC)* (IEEE, 2022), 311–318, <https://doi.org/10.1109/SYNASC57785.2022.00056>.
35. D. Herzog, W. Roland, C. Marschik, and G. Berger-Weber, "Comprehensive Surrogate Models for Predicting the Melt Conveying Characteristics of Channel Segments in High-Performance Single-Screw Extruders," *Polymer Engineering and Science* 66, no. 2 (2026): 716–738, <https://doi.org/10.1002/pen.70202>.
36. W. Roland, C. Marschik, B. Löw-Baselli, et al., "The Effect of Channel Curvature on the Flow Rate and Viscous Dissipation of Power-Law Fluids," in *Proceedings of the 76th Annual Technical Conference of the Society of Plastics Engineers (SPE ANTEC)*, vol. 4 (Society of Plastics Engineers, 2018), 3087–3093.
37. C. Marschik, W. Roland, M. Dörner, et al., "Leakage-Flow Models for Screw Extruders," *Polymers* 13, no. 12 (2021): 1919–1943, <https://doi.org/10.3390/polym13121919>.
38. C. Rauwendaal, *Polymer Extrusion*, 5th ed. (Hanser Publications, 2014).
39. M. Fernandez, M. E. Munoz, A. Santamaria, et al., "Determining the Pressure Dependency of the Viscosity Using PVT Data: A Practical Alternative for Thermoplastics," *Polymer Testing* 28 (2009): 109–113, <https://doi.org/10.1016/j.polymertesting.2008.09.008>.
40. M. Brillinger, B. Löw-Baselli, M. Prechtel, et al., "Verfahren zur Bestimmung der mechanisch eingebrachten Leistung in Extrudern," Austrian Patent 524053B1, 2022.

Supporting Information

Additional supporting information can be found online in the Supporting Information section. **Data S1:** Supporting Information.